Implementation and evaluation of SNICAR snow albedo scheme in Noah-MP (version 5.0) land surface model

Tzu-Shun Lin[1], Cenlin He[1], Ronnie Abolafia-Rosenzweig[1], Fei Chen[2], Wenli Wang[3], Michael Barlage[4], and David Gochis[1]

[1]NSF National Center for Atmospheric Research, Boulder, CO, USA

[2]Hong Kong University of Science and Technology, Hong Kong, China

[3]Institute of Atmospheric Physics, Chinese Academy of Sciences, Beijing, China

[4]NOAA/Environmental Modeling Center, College Park, MD, USA

Corresponding author: Tzu-Shun Lin (tslin2@ucar.edu)

Submitted to: Journal of Advances in Modeling Earth Systems (JAMES)

Key points

- We enhance Noah-MP snow albedo modeling by implementing physical snow radiative transfer and aging processes from the latest SNICAR
- The Noah-MP/SNICAR simulated snow albedo exhibits superior performance compared to the default snow albedo scheme at validation sites
- Noah-MP/SNICAR quantifies the impact of snow grain size, shape, and light-absorbing particles on snow albedo and radiative forcing

Abstract

The widely-used Noah-MP land surface model (LSM) currently adopts snow albedo parameterizations that are semi-physical in nature with nontrivial uncertainties. To improve physical representations of snow albedo processes, a state-of-the-art snowpack radiative transfer model, the latest version of Snow, Ice, and Aerosol Radiative (SNICAR) model, is integrated into Noah-MP in this study. The coupled Noah-MP/SNICAR represents snow grain properties (e.g., shape and size), snow aging, and physics-based snow-aerosol-radiation interaction processes. We compare Noah-MP simulations employing the SNICAR scheme and the default semi-physical Biosphere-Atmosphere Transfer Scheme (BATS) against in-situ snow albedo observations at three Rocky Mountain field stations. The agreement between simulated and in-situ observed ground snow albedo in the broadband, visible, and near-infrared spectra is enhanced in Noah-

MP/SNICAR simulations relative to Noah-MP/BATS simulations. The SNICAR scheme improves the temporal variability of modeled broadband snow albedo, with a nearly twofold higher correlation with observations (r=0.66) than the default BATS snow albedo scheme (r=0.37). The underestimated variability in Noah-MP/BATS is a result of inadequate physical linkage between snow albedo and environmental/snowpack conditions, which is substantially improved by the SNICAR scheme. Importantly, the Noah-MP/SNICAR model, with constraints of snow grain size from the MODIS snow covered area and grain size (MODSCAG) satellite data, physically represents and quantifies the snow albedo and absorption of shortwave radiation in response to snow grain size, non-spherical snow shapes, and light-absorbing particles (LAPs). The coupling framework of the Noah-MP/SNICAR model provides a means to reduce the bias in simulating snow albedo.

Plain Language Summary

Snow albedo, defined as the proportion of sun light reflected on the snowpack influences snowpack growth, melting rate, surface energy and water cycles, as well as regional and global hydrological and climate change. The community Noah-MP land surface model uses semi-physical snow albedo parameterizations with critical uncertainties. In this study, the integration of the latest version of the Snow, Ice, and Aerosol Radiative (SNICAR) model into Noah-MP aims to enhance the accuracy of snow albedo simulations. The coupled Noah-MP/SNICAR model encompasses various aspects of snow, including its grain properties, aging, and interactions among snow, aerosols, and radiation. We evaluate Noah-MP simulations using SNICAR and the default Biosphere-Atmosphere Transfer Scheme (BATS) snow albedo schemes against albedo observations at three Rocky Mountain stations. The SNICAR scheme enhances accuracy of snow albedo simulations, showing a correlation with observations that is twice as high as simulations using the default BATS snow albedo scheme. The variability of snow albedo in Noah-MP/BATS is underestimated due to the inadequate physical relationship between snow albedo and environmental/snowpack conditions. This issue is addressed and significantly improved by Noah-MP/SNICAR. It is worth noting that the Noah-MP/SNICAR model takes into account the constraints of fresh snow grain size from satellite data.

1. Introduction

Snow albedo is defined as the ratio of the snow-reflected solar radiation to the total solar radiation incident on the snowpack. The observed high snow albedo is a result of the considerable portion of the visible spectrum of solar energy on the snow surfaces (Cohen & Rind, 1991). The albedo of snow exerts a substantial influence on multiple facets in the Earth system, including the evolution of the snowpack, rates of melting, surface energy and water cycles, and regional and global hydrological and climate change (Barnett et al., 2005; Flanner et al., 2011; Qian et al., 2015; Skiles et al., 2018; Zhang et al., 2019). This can be attributed to the positive snow albedo feedback and the complex interactions that occur between the land and the atmosphere (Hall, 2004). Variations in snow albedo resulting from temperature warming or cooling can lead to

enhancements or reductions in the absorption of solar radiation, hence intensifying the initial warming or cooling (Thackeray & Fletcher, 2016).

There is still limitation and uncertainty in the representation of snow albedo processes within many land surface models (LSMs) coupled to regional and global weather and climate models, which consequently affects the estimation of land surface energy and water balances. For example, systematical snow albedo biases were found in one widely-used LSM, the Noah with multi-parameterization options (Noah-MP) (Niu et al., 2011) which is a land component within the Weather Research & Forecasting (WRF) model, the NOAA Unified Forecast System (UFS) model, and the National Water Model (NWM) among many others, as demonstrated by various studies (Abolafia-Rosenzweig et al., 2021, 2022a; Chen et al., 2014; He et al., 2019, 2021; Liu et al., 2021, 2022; Wang et al., 2020; Xiao et al., 2021). The snow albedo in Noah-MP is represented using semi-physical or empirical functions (Verseghy, 2007; Yang et al., 1997), which lack physical treatments of snow albedo response to the evolution of snow properties such as aging and metamorphism. This approach leads to an inconsistent treatment between snow albedo and other snowpack properties (He and Flanner, 2020). To enhance the accuracy of snow albedo modeling, it is necessary to have a comprehensive understanding of the underlying physical mechanisms that influence snow albedo. Subsequently, these processes need to be represented in a more physically realistic manner.

The albedo of snow is determined by a complex combination of multiple factors, such as snow depth, the size and shape of snow grains, and the concentration of light-absorbing particles (LAPs) (Warren and Wiscombe, 1980). It has been known that snow albedo is affected by LAPs mainly in the visible band (Warren and Wiscombe, 1980) and by grain size mainly in the near-infrared (NIR) band (Wiscombe and Warren, 1980). Following the occurrence of snowfall, snow crystals experience fast alterations in their size and shape, exhibiting a tendency for snow grains to progressively increase in size over time (Colbeck, 1982). The alteration in snow grain size influences the interaction between the snow surface and incoming solar radiation. The presence of larger grains in snow leads to an increase in the path length traveled by photons, resulting in a lower albedo (Warren 1982). The Snow, Ice, and Aerosol Radiative (SNICAR) model (Flanner et al, 2007, 2021) is one of the most widely used open-source snowpack radiative transfer models, which resolves the aforementioned physical processes and simulates snow albedo by considering snowpack properties such as grain size and shape, as well as environmental conditions including the presence of LAPs.

Simulating snow albedo using SNICAR has many advantages compared to the current semi-physical snow albedo schemes, such as the Biosphere-Atmosphere Transfer Scheme (BATS) in Noah-MP (Abolafia-Rosenzweig et al., 2022a; Yang et al., 1997). (1) The study conducted by Abolafia-Rosenzweig et al. (2022a) demonstrated the issue of using a constant parameter to represent the fresh snow albedo in Noah-MP/BATS, which is typically adopted by empirical/semi-physical schemes, whereas the measured albedo of fresh snow exhibits significant variability especially in the NIR band. In contrast, fresh snow albedo is influenced by several environmental conditions and physical processes in the SNICAR model, such as temperature, downward solar spectrum, snow grain size and shapes, LAPs within snow, and the thickness and density of the

snowpack. The SNICAR treatment is more physically realistic, as highlighted by Wang et al. (2020). (2) The inclusion of different snow grain shapes, such as spheres, spheroids, hexagonal plates, and Koch snowflakes, is necessary to depict the types of non-spherical snow grains that are commonly observed (Liou et al., 2014; He et al., 2018a, 2023a; Robledano et al., 2023). This representation is currently absent in Noah-MP, while it has been included in SNICAR. (3) The representation of snow aging processes is empirical and incomplete in Noah-MP due to the absence of the simulation of snow grain size. Instead, the simulated snow grain size in SNICAR can be validated using either in-situ measurements or remote-sensing products. This approach offers the advantage of requiring less arbitrary tuning of empirical snow aging parameters which is needed by current Noah-MP snow albedo schemes. (4) SNICAR simulates the interaction between snow, aerosols, and radiation (Flanner et al., 2021; He et al. 2018a; Skiles & Painter, 2019), encompassing three LAPs: black carbon (BC), organic carbon (OC), and dust. Additionally, the latest SNICAR coupled into the Community Land Model (CLM5) and the DOE's Energy Exascale Earth System Model (E3SM) Land Model (ELM) also includes the internal mixing of BC and dust with snow grains (He et al., 2023a; Hao et al., 2023). However, these treatments are either missing or not physically represented in Noah-MP. (5) SNICAR presents the effect of solar zenith angle on snow albedo (for direct radiation) physically, while Noah-MP parameterizes this effect semi-empirically such as in BATS. (6) SNICAR computes vertical solar radiation absorption and heating rate for individual snow layers and the top soil layer, which changes snow and soil temperature profiles but is missing in the current Noah-MP albedo schemes. (7) SNICAR has a hyperspectral calculation capability that is more accurate than narrowband calculations (Wang et al., 2022), and can be expanded to incorporate or compare with spectral radiation obtained by remote sensing, while current Noah-MP snow albedo schemes only use two (visible and NIR) bands.

Recent studies have implemented SNICAR in some LSMs coupled to global climate models, such as the CLM within Community Earth System Model (CESM) (Flanner et al., 2007; He et al., 2023a) and the DOE's ELM (Hao et al., 2023). This study aims to implement the latest SNICAR version that has several new features and enhancements (He et al., 2023a) into the newly refactored Noah-MP version 5 by accounting for snow grain shape, size, snow-aerosol-radiation interaction, and snow aging processes (Section 2), and to evaluate modeled snow albedo using in situ albedo observations at three Rocky Mountain field stations (Section 3). We use in situ observations of upward/downward shortwave radiation and snow depth and satellite-derived snow grain size to evaluate and constrain the modeled snowpack and radiation conditions. We first evaluate whether the coupled Noah-MP/SNICAR model can accurately reproduce the observed mean and variability of snow albedo, and then perform the process-level model experiments to quantify the effects of snow grain size, shape, and LAPs on snow albedo and radiative forcing (Section 4). We also compare the snow albedo between enhanced Noah-MP/SNICAR simulation and the default Noah-MP/BATS simulation (Section 4). Section 5 discusses the potential uncertainties and future directions, and Section 6 concludes the study.

2. Noah-MP and its coupling with SNICAR

2.1. Noah-MP model description

Noah-MP (Niu et al., 2011; Yang et al., 2011) is one of the most widely used open-source community LSMs worldwide, which has been used in various research and operational models pertaining to weather, climate, and hydrology. The newest version of Noah-MP (version 5.0) (He et al., 2023c) has undergone recent refactoring and incorporating contemporary Fortran code styles, data structures, and standards. This refactoring has significantly improved the model's modularity, interoperability, and applicability (He et al., 2023b).

Noah-MP is featured as a multi-parameterization LSM that enables the user to combine different physics schemes for modeling individual land surface processes (Niu et al. 2011). The Noah-MP snow module has the capability to simulate a maximum of three snow layers, with the number of layers being dependent on snow depth. Noah-MP treats explicit snow layers when snow depth is larger than 2.5 cm, and implicitly represents a very shallow (<2.5 cm) snow layer by combining it with the top soil layer in energy and water balance calculations. Snow layer temperature, snow depth, and snow water and ice contents are calculated based on snowpack water and energy balances. The model considers many key snow processes such as snow layer division and combination, liquid water holding within the snowpack, snow compaction, snow melting and refreezing, frost and sublimation at the ground snow surface, and the interception of snow by vegetation. The technical report by He et al. (2023c) provides a comprehensive description of the various aspects related to snowpack mass and energy processes.

Within Noah-MP, there exist two semi-physical snow albedo schemes, namely CLASS (Verseghy, 2007) and BATS (Yang et al., 1997). The mathematical equations of the two snow albedo schemes are described in detail in He et al. (2023c). Both schemes simulate snow albedo in the visible and NIR bands under direct and diffuse radiation, but CLASS assumes the same snow albedo for direct and diffuse radiation as well as visible and NIR bands, which is physically unrealistic. Furthermore, both schemes do not explicitly simulate the evolution of snow properties (e.g., snow aging/metamorphism, grain size, and shape). A recent study (Abolafia-Rosenzweig et al., 2022a, 2022b) has tried to optimize the BATS albedo parameters using in-situ snow albedo measurements, which however still showed nontrivial remaining biases particularly for fresh snow albedo due to a lack of physical representation of relevant albedo processes.

2.2 Noah-MP/SNICAR coupling

In this study, we couple the refactored Noah-MP version 5 with the latest version of SNICAR (https://github.com/ESCOMP/CTSM/pull/1861) that has recently been implemented into CLM5 (He et al., 2023a).

2.2.1 Multiple physics options for SNICAR albedo calculations

The SNICAR scheme we implement into Noah-MP incorporates several key physical processes and updates following He et al. (2023a): (1) two options for radiative transfer solvers, with one for a traditional tri-diagonal matrix two-stream solver (Toon et al., 1989) and one for a new adding-doubling solver (Dang et al., 2019); (2) three options for ice optical properties (Flanner

et al., 2021) using different ice refractive indices from Warren (1984), Warren and Brandt (2008), and Picard et al. (2016); (3) updated aerosol optical properties of BC and OC from Flanner et al. (2021); (4) six options of downward solar spectra for multiple atmospheric conditions (Flanner et al., 2021), including mid-latitude winter, mid-latitude summer, sub-Arctic winter, sub-Arctic summer, Summit Greenland, and high mountain; (5) four types of snow grain shapes including sphere, spheroid, hexagonal, and snowflake (He et al., 2017); (6) three dust types including Saharan dust, Colorado dust, and Greenland dust (Flanner et al., 2021); (7) two options for either internal or external mixing of dust (He et al., 2019b) or BC (He et al., 2017) with snow grains; (8) two options for wavelength band setup, including 5-band and hyperspectral (480-band with 10-nm spectral resolution) capabilities. Both 5-band and 480-band albedo results are then averaged to two (visible and NIR) bands' values to be used in Noah-MP surface energy flux calculations. We implement all these SNICAR albedo calculation processes and the ability of choosing different physics options to simulate each individual processes into Noah-MP.

2.2.2 Model inputs

We incorporate additional input datasets that are required for SNICAR (Flanner et al., 2021; He et al., 2023a) through an updated model I/O interface. SNICAR requires the input variables including direct/diffuse radiation, surface downward solar spectrum, solar zenith angle (only for direct radiation), albedo of the surface underlying snowpack, vertical profiles of snow grain size, snow layer thickness, snow density, and mass concentrations of LAPs (BC, mineral dust, and OC), snow grain shape, and optical properties of ice and LAPs. The optical properties of ice and LAPs for each snow layer and spectral bands, including single-scattering albedo, mass extinction cross section, and asymmetry parameter, are archived as look-up table datasets derived by Flanner et al. (2021) and He et al. (2023a).

2.2.3 Snow grain size and aging processes

The evolution of snow effective grain size is represented by snow aging processes and implemented into the Noah-MP/SNICAR model. The change in effective snow grain size is based on the dry and wet snow processes, including liquid-water-induced metamorphism, dry snow metamorphism, refreezing of liquid water, and the addition of freshly fallen snow (Flanner et al., 2007; Lawrence et al., 2019). The liquid-water-induced metamorphism is parameterized based on measured grain growth rates under different liquid water contents (Brun, 1989). The dry snow metamorphism is determined by snow temperature, temperature gradient, density, and initial snow grain size distribution based on a microphysical particle model that simulates diffusive vapor flux amongst collections of ice crystals with various size and inter-particle spacing (Flanner and Zender, 2006). This process reproduces the typical observed rapid snow aging and increased snow grain size under the conditions of combined warm snow, large temperature gradient, and low density. The effective radius of refrozen liquid water is set to 1000 μm (Oleson et al., 2013). The air temperature is a key factor in determining the grain size of freshly fallen snow. At temperatures below -30 degrees Celsius, a minimum of 54.5 μm (radius) is imposed (Lawrence et al., 2019). A limit is imposed on the maximum of 204.5 μm (radius) when the temperature exceeds 0 degrees Celsius. A linear ramp is employed within the temperature range between -30 to 0 degrees Celsius (Lawrence et al., 2019). These maximum and minimum limits are tunable parameters. In our

investigation, we discover that grain size and snow albedo are sensitive to the minimum and maximum values of the grain size of freshly fallen snow. In Section 3.3.3, we have optimized these two parameters to match with the snow grain size acquired from a satellite product (see Section 3.2). In situations where there is a non-zero snow mass but an explicit snow layer has not yet been established (i.e., snow depth <2.5 cm), the effective snow grain size is assigned as the effective radius of freshly fallen snow (Lawrence et al., 2019). When snow layers are combined or divided, the effective snow grain size is calculated as a mass-weighted mean of those of the two layers. Lastly, the effective snow grain size is limited to a range of 30-1500 μm, as this range covers the majority of snow grain size in reality and corresponds to the defined optical properties that are archived in look-up tables (Flanner et al., 2021; He et al., 2023a).

2.2.4 Snow-aerosol-radiation interactions

Additionally, we implement a mass-conserving approach to account for the presence of LAPs within snow, encompassing the mechanisms of atmospheric aerosol deposition on the uppermost snow layer, aerosol mass reduction via inter-layer meltwater drainage, and aerosol mass changes due to snow layer combination and subdivision (Flanner et al., 2007; Lawrence et al., 2019). The Noah-MP/SNICAR model tracks the mass of nine aerosol particle species within each snow layer including hydrophilic BC, hydrophobic BC, hydrophilic OC, hydrophobic OC, and mineral dust with five particle size bins (μm in diameter, Table S2): 0.1-1.0, 1.0-2.5, 2.5-5.0, 5.0-10.0, and 10.0-100.0 (Flanner et al., 2021). Each species exhibits distinct optical characteristics (Flanner et al., 2021; He et al., 2023a) and meltwater removal efficiencies (Lawrence et al., 2019).

2.2.5 Albedo output and snowpack heating

The results simulated from the Noah-MP/SNICAR model include the spectral snow albedo and the fraction of solar flux that is absorbed by each individual snow layer and the top soil layer. The spectral snow albedo is partitioned into visible and NIR bands by computing the spectrally weighted mean based on downward solar spectra (Flanner et al., 2007). The layer-wise snowpack heating due to snow and LAPs absorption of solar radiation from SNICAR is coupled with Noah-MP snow and soil temperature computations to alter the temperature for each snow layer and the underlying top soil layer.

3. Model experiments and evaluation data

3.1 In-situ observations

In-situ observations of snow albedo and snow depth data are obtained from three high-elevation locations, East River, Irwin, and Senator Beck, within the southern Rocky Mountains in the state of the Colorado, United States (Figure 1; Abolafia-Rosenzweig et al., 2022a, 2022b). The longitudes, latitudes, elevation, vegetation types, available observed spectrum bands of snow albedo (broadband, visible, and NIR), and atmospheric forcing variables for each site are provided in Table S1. The comprehensive methodologies for measuring solar radiation, albedo and snow depth can be found in Abolafia-Rosenzweig et al. (2022a).

The snow albedo and snow depth measurements have undergone rigorous quality control procedures to ensure their accuracy and reliability. To eliminate the effect of low sun angle on albedo, we use averages of albedo and snow depth measured between 11:00 and 13:00 local time for the three sites during the periods of investigation. The analysis is further limited to periods when the observed snow depth is more than 0.5 m at the East River site and 0.2 m in the Senator Beck and Irwin sites, in order to ensure that understory vegetation is completely buried by snowpack to eliminate the influence of vegetation on snow albedo, following Abolafia-Rosenzweig et al. (2022a). Observed albedo values that exceed 1.0 or fall below 0.0 are removed.

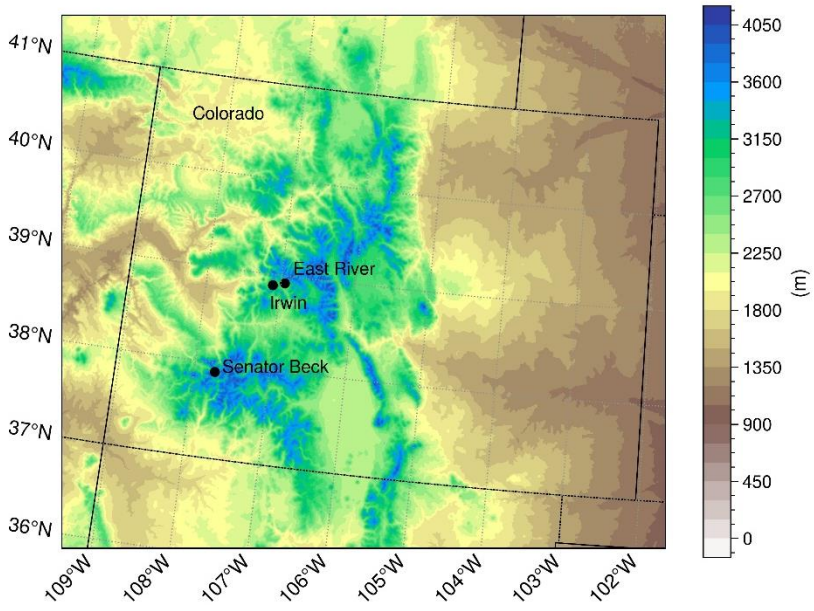

Figure 1. Locations of the three study sites with topography.

3.2 MODIS snow covered area and grain size (MODSCAG) product

We use a daily 463-m MODSCAG product (Painter et al, 2009) to evaluate and optimize modeled snow grain size. Based on spectral unmixing and physically based snow radiative transfer models that remove soil and vegetation portions of the observed pixel, MODSCAG provides snow grain size at roughly 10:30 LST (local solar time). For a clear sky day, the mean absolute error (MAE) for snow grain size from MODSCAG compared to field measurements at a single site is 51 μm (Painter et al., 2009). For both clear and cloud sky days, the gap-filled MODSCAG has a root mean square error (RMSE) of 118 μm for snow grain size compared to observations at three sites in the western United States (Bair et al., 2019). The MODSCAG data are obtained from the University of California, Santa Barbara (UCSB) website at https://snow.ucsb.edu/products/MODSCAG/WUS/. The snow grain size values are extracted from the encompassing MODSCAG grid cell of the three field sites studied in this work.

297

298 3.3 Site-specific model setup and simulations

299 Noah-MP simulations adopt model-physics settings from the options used in continental-
300 scale convection-permitting WRF/Noah-MP climate simulations (He et al., 2019a; Liu et al., 2017;
301 Rasmussen et al., 2023) that have reasonably captured key land surface states and fluxes over the
302 continental U.S., except for different snow albedo options tested in this study. The snow-related
303 parameters within Noah-MP follows the values used in the latest release of Noah-MP version 5.0
304 (He et al., 2023c). Leaf area index (LAI) is characterized by vegetation type based on a 10-yr
305 monthly climatology of MODIS products (Yang et al., 2011). The vegetation type for each
306 research site is grassland, and the canopy height is set as documented at each specific site
307 (Abolafia-Rosenzweig et al., 2022a). For each study site, Noah-MP is first spun up for 11-13 years
308 to get the steady-state as listed in Table S1, followed by model analysis for subsequent years
309 (Abolafia-Rosenzweig et al., 2022a). The analysis period ranges between October 2018 to August
310 2021 in Irwin, October 2011 to 2020 October in Senator Beck, and July 2017 to November 2019
311 in East River.

312 3.3.1 Atmospheric forcing

313 The Noah-MP simulations utilize atmospheric forcing derived from a combination of two
314 sources: the hourly forcing data obtained from the 1-km observation-constrained NOAA's
315 Analysis of Record for Calibration data set (AORC; National Weather Service, 2021) which are
316 then replaced with in-situ observed data when accessible from each study site. The atmospheric
317 forcing variables observed at each location are listed in Table S1. To minimize simulation
318 uncertainty due to downward direct/diffuse shortwave radiation in visible and NIR bands, we use
319 both the observed total downward shortwave radiation and the observed fraction of direct/diffuse
320 and visible/NIR radiation when observational data are available.

321 3.3.2 Aerosol deposition flux

322 All model simulations are driven by the hourly aerosol (BC, dust, and OC) wet and dry
323 deposition fluxes from the MERRA-2 reanalysis (Randles et al., 2017). MERRA-2 provides the
324 wet and dry deposition fluxes for hydrophobic and hydrophilic (aged) OC and BC as well as dust
325 with 5 size bins at a spatial resolution of 0.625°×0.5°. The aerosol deposition fluxes at three in-
326 situ locations are determined by spatial interpolation based on the nearest neighbor grids of
327 MERRA-2 values. Additionally, the sizes of MERRA-2 dust aerosol are converted to size bins that
328 are compatible with those in Noah-MP/SNICAR (Table S2).

329 3.3.3 Fresh snow grain size optimization

330 We optimize the tunable minimum and maximum values of freshly fallen snow grain size
331 in SNICAR by comparing the simulated snow grain size to the MODSCAG data (Section 3.2). We
332 define the fresh snow cases based on the following criteria: 1) a daily observed increment of snow
333 depth exceeding 0.02 m following Abolafia-Rosenzweig et al. (2022a); 2) a precipitation amount
334 surpassing 0.0 mm/day following Wang et al. (2020); and 3) the model simulation indicates a
335 complete (100%) snow cover fraction. The original values are 54.526 μm for the minimum and

204.526 μm for the maximum. In this study, the minimal value is optimized to 33.0 μm, which is determined by identifying the smallest snow grain size from the MODSCAG data across all study sites and study periods. The maximum value is optimized to 91.0 μm to match modeled average snow grain size with the MODSCAG averaged value over all study sites and study periods.

3.3.4 Model experiments

We conduct five model experiments, as shown in Table 1. The first simulation (Exp1) serves as the baseline case using the SNICAR snow albedo scheme. The SNICAR configuration includes the utilization of an adding-doubling solver, a midlatitude winter atmosphere profile with five wavelength bands, a hexagonal snow grain shape, the Colorado dust type, ice optical properties obtained from Picard et al. (2016), the inclusion of BC, dust, and OC, and the internal mixing of BC and dust with snow grains. Additionally, the simulation incorporates optimized parameters with respect to the fresh snow grain size mentioned in Section 3.3.3. Subsequently, we perform four sensitivity simulations (Exp2-5) to comprehend the impacts of snow grain size, snow grain shapes, and LAPs on snow albedo and surface radiative balance. The second simulation (Exp2) is identical to Exp1, except that it employs the original SNICAR parameters for fresh snow grain size. The third simulation (Exp3) is identical to Exp1, except for the modification of the hexagonal snow grain shape to the spherical shape. The fourth simulation (Exp4) is identical to Exp1, except that it does not account for the influence of LAPs in snow. The final simulation (Exp5) utilizes the default Noah-MP BATS snow albedo scheme instead of SNICAR. All simulations are forced with the in-situ observed snow depth to reduce the albedo uncertainty introduced by snow depth bias, as previous studies have shown nontrivial snow depth bias simulated by Noah-MP (Abolafia-Rosenzweig et al., 2021; Chen et al., 2014; He et al., 2019a; 2021; Ikeda et al., 2021). Specifically, the observed snow depth is directly inserted to ensure the simulated snow depth aligns with the observed values during periods when observations are available (Figure S1). The snow depth is subsequently transformed into snow water and ice by multiplying with the modeled snow density, as typically done in snow depth data assimilation procedures. We note that this may introduce uncertainty to snow water equivalent in the model due to the lack of direct observations of snow density.

Table 1. Noah-MP model configurations for different experiments.

Experiments	Snow albedo scheme	Snow grain size	Snow shape	Snow impurities
Exp1 (baseline)	SNICAR	Optimized	Hexagonal	w/ LAPs
Exp2	Same as Exp1	Original	Same as Exp1	Same as Exp1
Exp3	Same as Exp1	Same as Exp1	Sphere	Same as Exp1
Exp4	Same as Exp1	Same as Exp1	Same as Exp1	w/o LAPs
Exp5	BATS	-	-	-

3.4 Evaluation metrics

Statistical metrics are computed to assess the performance between simulated and observed snow albedo. Bias is employed as a metric to assess the extent to which the modeled albedo is capable of properly replicating the average condition of the observed values. The root mean square error (RMSE) is employed as a metric to assess the accuracy of the model capability in estimating the observed value. The Pearson's correlation coefficient (r) is used to quantify the temporal correlation of modeled and observed snow albedo.

4. Results

4.1 Model evaluation

4.1.1 Snow grain size

The Noah-MP/SNICAR simulation using original SNICAR grain size parameters (i.e., Exp2) produces systematically higher fresh and aged snow grain sizes by about two times compared to MODSCAG (Figure 2). This discrepancy can be attributed to the overestimate of fresh snow grain size. When optimizing the size parameters of the freshly fallen snow grains (i.e., Exp1; see Section 3.3.3), the modeled average fresh snow grain sizes (85 μm) at three research sites agree very well with the values (85 μm) obtained from MODSCAG (Figure 2). Additionally, our results demonstrate that by improving the fresh snow grain size simulation in Noah-MP/SNICAR, we can further effectively decrease the bias in the simulated aged (non-fresh) snow grain size. The mean value of the modeled aged snow grain size decreases from 182 to 103 μm, which matches very well with the observed value of 101 μm (Figure 2).

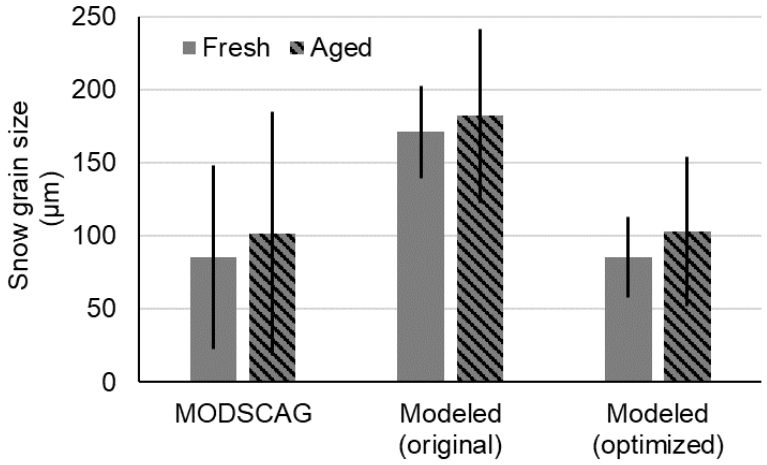

Figure 2. Comparison of the average fresh and aged snow grain size obtained from MODSCAG, and the simulated results from Noah-MP/SNICAR simulations with the original and optimized fresh snow grain size parameters at three study sites during the periods when MODSCAG data is accessible. The uncertainty bar represents the spatiotemporal variability of snow grain size within one standard deviation. The fresh snow is defined in Section 3.3.3.

395

396 **4.1.2 Snow albedo during all periods**

397 Overall, the Noah-MP/SNICAR baseline simulation (i.e., Exp1) captures the observed
398 snow albedo values, but with a higher broadband albedo by about 0.072 and less temporal
399 variability (Figure 3a-c). The broadband overestimates mainly arise from the overestimated visible
400 snow albedo by about 0.086, likely caused by the uncertainty in aerosol deposition and/or snow
401 density, because snow grain size and snow depth are constrained by observations. This also
402 explains the good agreement between modeled and observed mean NIR snow albedo (Figure 3a-
403 c), since NIR snow albedo is sensitive to grain size. Uncertainty in snow grain shape could also
404 slightly (by up to ~0.02) contribute to the overestimated visible snow albedo based on sensitivity
405 analysis (Section 4.2.2). The missing treatment of small-scale snow surface roughness in the model
406 could also contribute to the snow albedo overestimates (Manninen et al., 2021), but it generally
407 has a stronger impact on NIR albedo and hence may not be the main culprit here. Nevertheless,
408 the model reproduces the observed pattern of the visible albedo larger than the NIR albedo. The
409 underestimated temporal variability of snow albedo at both visible and NIR bands is partially
410 caused by the underestimated variability of snow grain size (Figure 2), particularly during ablation
411 periods (Figure 3g-i). This is mainly due to the uncertainty in snow aging processes, which are less
412 constrained by observations. The uncertainty in aerosol deposition and evolution in snow could
413 also contribute to the underestimated visible albedo temporal variability because the visible snow
414 albedo is more sensitive to snow impurity than snow grain size (Section 4.2.3).

415 **4.1.3 Fresh snow albedo**

416 The Noah-MP/SNICAR baseline simulation of broadband fresh-snow albedo reproduces
417 the mean and variability of observations due to the well-captured fresh snow grain size (Figure 2),
418 with higher accuracy in the Senator Beck and Irwin sites than East River sites (Figure 3d-f). The
419 simulated median broadband value closely matches the value of observed fresh-snow albedo at the
420 Senator Beck site (0.88 observed vs. 0.87 modeled) and the Irwin site (0.84 observed vs. 0.83
421 modeled). At the East River site, the modeled median value (0.83) is higher than the observed
422 values (0.76) with underestimated temporal variability. For the visible band, the median fresh snow
423 albedo is slightly overestimated by 0.03 at both Senator Beck and Irwin sites (Figure 3d-e). For
424 the NIR band, the median fresh snow albedo is underestimated by about 0.03 at the Senator Beck
425 site and about 0.07 at the Irwin site. Thus, low broadband biases at Irwin and Senator Beck are
426 attributable to compensatory errors in visible and NIR bands.

427 **4.1.4 Snow albedo during melting periods**

428 We evaluate snow albedo during the melting period, which is delineated as the time
429 spanning from March to June (Figure 3g-i). As snow melts, its albedo decreases with increased
430 temporal variability in comparison to fresh snow albedo. The simulated snow albedo generally
431 captures the observations during melting periods at broadband, visible, and NIR bands, with a
432 similar bias pattern as that of the entire snow period (Figure 3a-c). Specifically, the overestimated
433 broadband albedo (by 0.066) is dominated by the overestimate in the visible band (mean bias =
434 0.093), with NIR albedo better simulated (mean bias = 0.043). This is likely due to the uncertainty

in aerosol content in snow, snow density, and/or snow grain shape as discussed in Sections 4.1.2 and 5. The underestimated temporal variability of snow albedo at all bands can be explained by the uncertainty in snow aging processes and aerosol content in snow as mentioned in Section 4.1.2.

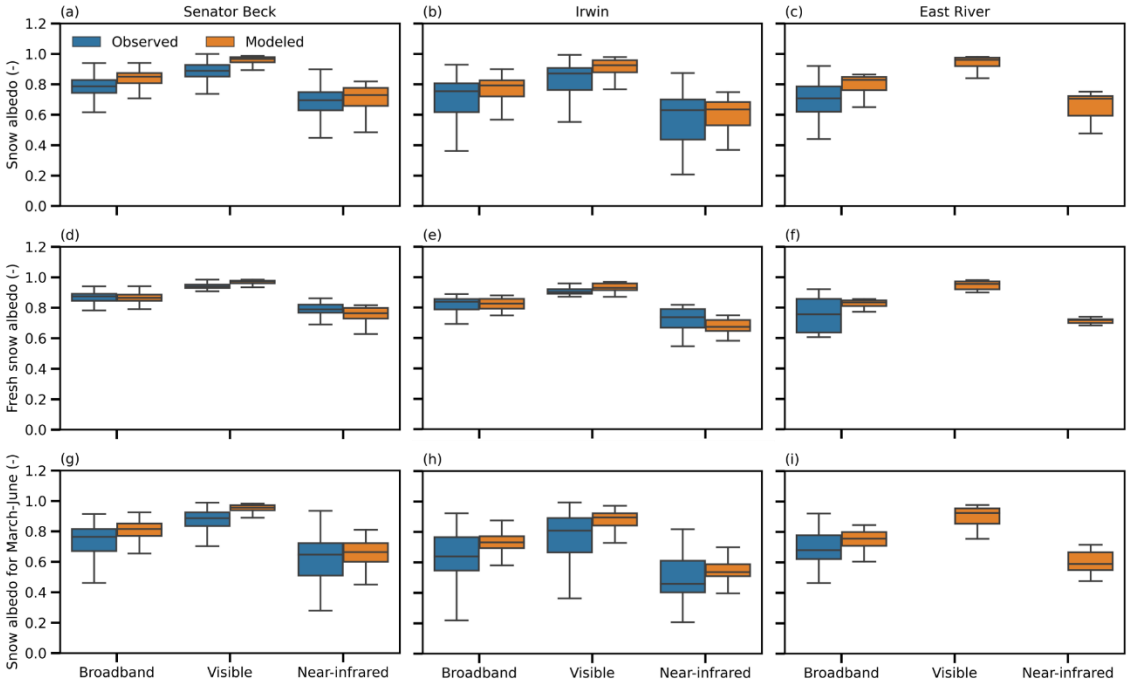

Figure 3. Site-level comparisons of snow albedo (a-c), fresh snow albedo (d-f), and snow albedo over the melt period (March-June) (g-i) from observations (Observed) and Noah-MP/SNICAR simulations (Modeled) at the Senator Beck (left panels), Irwin (middle panels), and East River (right panels) stations. The boxes are the interquartile ranges, the horizontal lines plotted in the boxes are the median values, and the whiskers indicate the maximum and minimum values of the results.

4.1.5 Comparison with default Noah-MP/BATS snow albedo scheme

We further compare the Noah-MP/SNICAR simulation with the Noah-MP simulation using the default semi-physical BATS snow albedo scheme that has been recently optimized by Abolafia-Rosenzweig et al. (2022a). Overall, the Noah-MP/SNICAR results outperform those of Noah-MP/BATS at all three sites (Figure 4). The SNICAR scheme improves the temporal variation (*slope* in the scatter plots) and correlation (*r* in scatter plots) with the observations for snow albedo at all bands. We note that the underestimated variability in the Noah-MP/BATS snow albedo suggests inadequate physical linkage and sensitivity between snow albedo and environmental/snowpack conditions in the BATS scheme, which is substantially improved by the SNICAR scheme. In terms of mean *Bias* and *RMSE*, there are few variations between the two simulations for the Senator Beck and East River sites, while the Irwin site shows a significant

improvement (about 50%). Noah-MP/SNICAR improves the issue of conditional bias existing in Noah-MP/BATS, i.e., the tendency of underestimating high albedo values and overestimating low albedo values. SNICAR enhances the variability in the visible snow albedo, which mitigates the overestimate of visible snow albedo in BATS. In the Noah-MP/BATS simulation, the visible snow albedo is consistently around 0.9 (blue dots in Figure 4b and 4e), which is not realistic. This could be because the BATS scheme uses a fixed parameter for fresh snow albedo (Abolafia-Rosenzweig et al., 2022a; Wang et al., 2020). However, in the Noah-MP/SNICAR simulation, the fresh snow albedo is dynamically dependent on environmental conditions such as changes in temperature, snow depth, snow grain size, and the concentrations of LAPs. Furthermore, the simulation of NIR snow albedo is significantly improved by Noah-MP/SNICAR relative to Noah-MP/BATS, leading to a notable decrease in the variability bias and bringing the simulated values much closer to the observed ones.

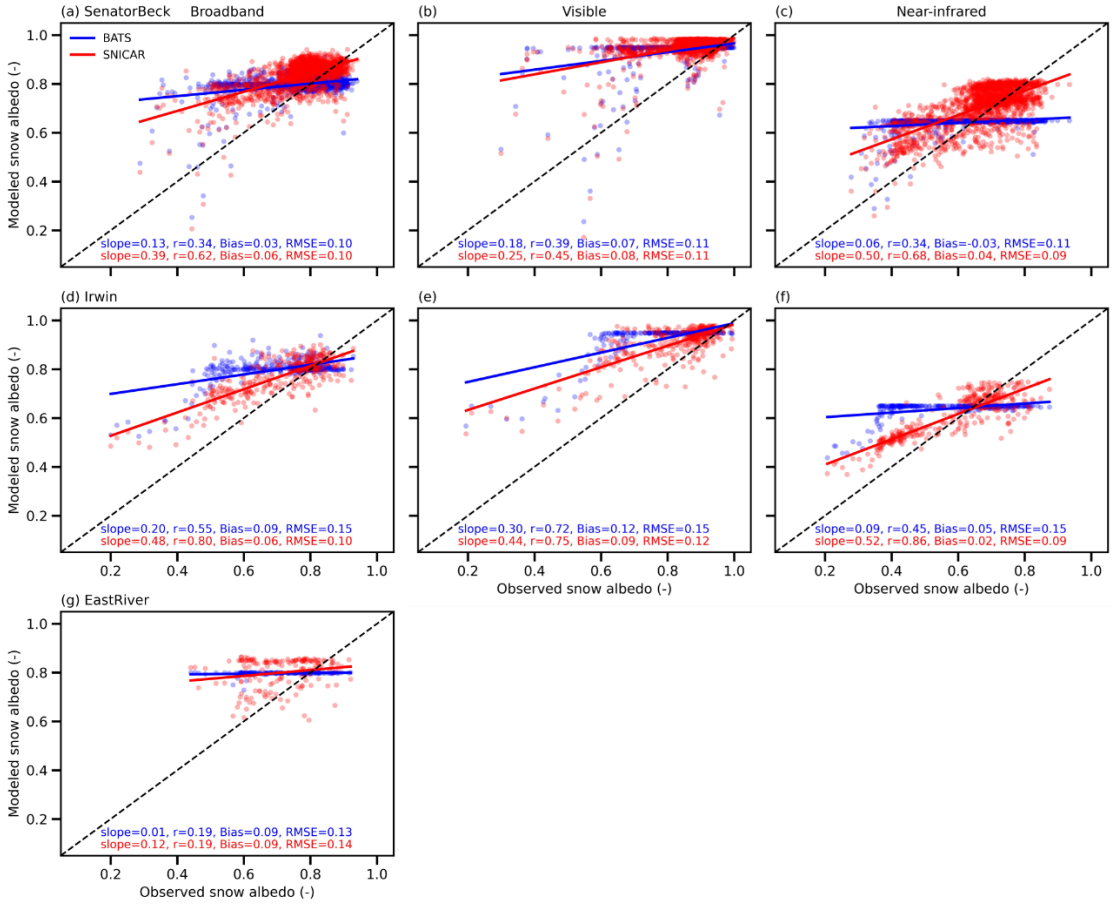

Figure 4. Scatter plots comparing observed, Noah-MP/BATS (blue dots), and Noah-MP/SNICAR (red dots) simulated ground snow albedo in broadband (a, d, and g), visible (b and e), and near-infrared (c and f) wavelengths at the Senator Beck (top panels), Irwin (middle panels), and East River (bottom panels) stations.

4.2 Effects of snow grain size, snow shape, and LAPs on albedo and radiative forcing

Here, we quantify the modeled snow albedo and absorbed solar radiation in response to key snow albedo factors in Noah-MP/SNICAR simulations.

4.2.1 Snow grain size

The optimization of fresh snow grain size parameters (Section 3.3.3) leads to a decrease in snow grain size, which better agrees with observations (Figure 2) and in turn increases snow albedo (Figure 5a-c). The broadband snow albedo at the Senator Beck, Iwrin, and East River sites increases on average by 0.022, 0.012, and 0.021, respectively. The albedo changes induce surface radiative forcing (SRF) values of -14.1, -6.4, and -12.8 W m^{-2} (Figure 6a-c). The changes in snow grain size have a more pronounced impact on the NIR band compared to the visible band, which is consistent with previous studies showing higher NIR snow albedo sensitivity to snow grain size (e.g., Flanner et al., 2021). As a result, there are greater fluctuations in the SRF in the NIR band, leading to a decrease in the absorbed broadband solar radiation. In addition, the albedo and SRF changes induced by snow grain size changes are more pronounced for fresh snow compared to those in the melting period, mostly due to alterations in the fresh snow grain size by the parameter optimization.

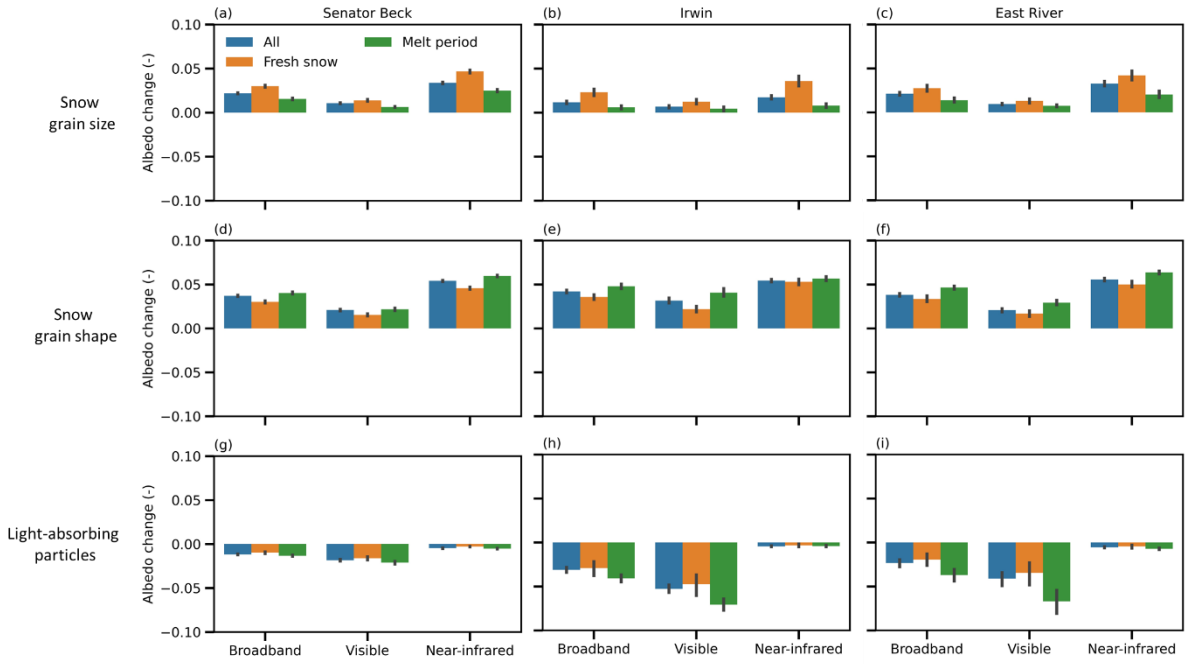

Figure 5. Changes in snow albedo due to changes in snow grain size from original fresh snow grain parameters to optimized ones (a-c), snow grain shape from sphere to hexagonal shape (d-f), and light-absorbing particles (LAPs) from no LAPs to with LAPs (g-i) in three stations, Senator Beck (left panels), Irwin (middle panels), and East River (right panels). The error bars represent the range of values within one standard deviation of temporal variability. The color of the plots

represents the data for the entire snow season (All), as well as the cases for fresh snow and the melting period (March-June).

4.2.2 Snow grain shape

In contrast to a spherical shape, a hexagonal grain shape exhibits a greater snow albedo (Figure 5d-f) and a lower SRF (Figure 6d-f). This is because non-spherical grains have a smaller asymmetry factor and weaker forward scattering compared to their spherical counterparts (Dang et al., 2016; He et al., 2017; 2018b), which is more representative of real-world conditions (Flanner et al., 2021; Hao et al., 2023; He et al., 2023a). The broadband snow albedo in the Senator Beck, Irwin, and East River stations increases by an average of 0.037, 0.042, and 0.038, respectively. This increase in albedo results in changes in surface solar radiation absorption of -26.7, -29.8, and -25.8 W m^{-2}. During the melting period, the influence of the snow non-sphericity has a greater impact on snow albedo and SRF compared to the time when the snow is fresh, due to the larger snow grain size and shallower snowpack during melting periods (He et al., 2018b; He, 2022). Although the rise in albedo and the decrease in SRF occur in both the visible and NIR bands, it is more pronounced in the NIR band, because the NIR albedo is more sensitive to snow grain shape (Dang et al., 2016; Flanner et al., 2021).

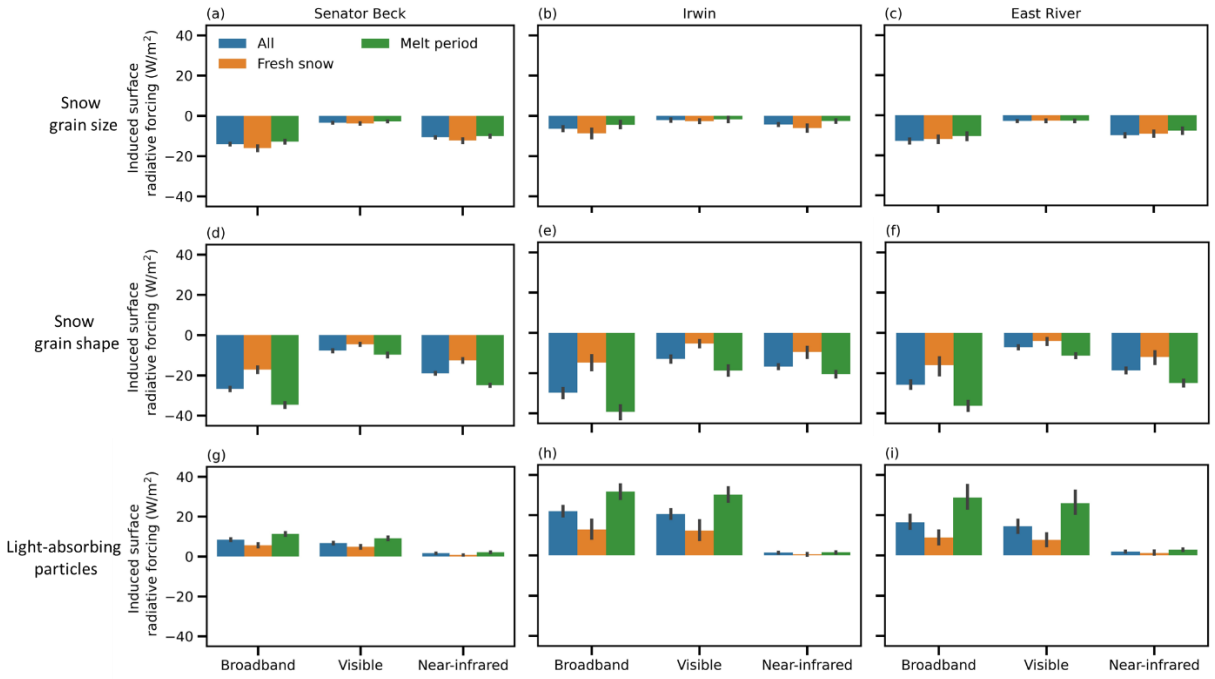

Figure 6. Similar to Figure 5, but for the induced surface radiative forcing (SRF).

4.2.3 Light-absorbing particles

Figures 5g-i and 6g-i display the changes in snow albedo and SRF caused by the LAPs, respectively. Overall, including LAPs in snow causes a decrease in the broadband snow albedo by an average of -0.012 at the Senator Beck station. This reduction in albedo results in a SRF of 8.4 W m^{-2}. The Irwin and East River sites exhibit greater changes in snow albedo and SRF compared to the Senator Beck site, mostly due to the higher concentrations of LAPs present in these two locations. The LAPs-induced SRF at the Irwin station is 21.9 W m^{-2}, while in the Easter River station it is 16.4 W m^{-2}. These changes correspond to a decrease in the broadband snow albedo of -0.031 in the Irwin station and -0.023 in the Easter River station. The effects of LAPs are much more pronounced in the visible band than the NIR band, consistent with literature (e.g., Warren and Wiscombe, 1980; Flanner et al., 2007). The melting period exhibits greater LAPs-induced changes in snow albedo and SRF compared to the fresh snow period, because of larger snow grain sizes and higher snowpack density during melting periods (Flanner et al., 2021; He, 2022) as well as the enrichment of LAPs as snow melts (Niu et al., 2017). In addition, the higher downward solar radiation during melting periods also contributes to the higher SRF compared to winter.

5. Uncertainty discussions and future directions

Snow grain shape, size, and snow LAPs all contribute to the potential uncertainty in snow albedo calculations and solar radiation processes. In the three study sites, the shape of snow grains has a considerable impact on snow albedo over the whole snow season. However, because there is no model process that accounts for the dynamic evolution of snow grain morphologies and no direct observational constraints, the model's assumption of non-spherical shape throughout the period is uncertain (He et al., 2023a). In reality, the shape of snow grains demonstrates geographical variation and temporal variability, which necessitates additional refinements (Hao et al., 2023). During the melting phase, the snow albedo biases and the effects of LAPs on snow albedo are stronger than during the accumulation period (i.e., fresh snow). Nonetheless, the coarse resolution of the MERRA-2 aerosol deposition data is accompanied by uncertainty. Furthermore, the LAPs associated with snow are influenced by tunable model parameters such as snow aging scaling factor and inter-layer melt-water scavenging efficiency factor, both of which affect the size evolution of snow grains and the concentrations of LAPs within the snow through positive feedback mechanisms (Qian et al., 2014). Because of the lack of direct observed data, these model parameters are poorly constrained and warrant further exploration to reduce uncertainty in calculating the interactive effects of grain size and snow LAPs on snow albedo particularly during melting period.

Furthermore, it is important to acknowledge that the input data, such as atmospheric forcing, are fundamental yet unavoidable sources of uncertainties. We strive to utilize in-situ observed forcing data to the greatest extent possible in order to decrease the level of uncertainty. In Noah-MP, certain snowpack physical processes, such as densification, still have uncertainties (e.g., He et al., 2019, 2021), which may contribute to the bias in the estimation of snow albedo. To mitigate this uncertainty, we used observed snow depth data to constrain model simulations. Looking beyond this study, we plan to evaluate over a larger study domain and conduct regional simulations in a coupled land-atmosphere modeling system to assess the feedback induced by the

563 enhanced SNICAR snow albedo scheme, such as the western United States that experience burning
564 or/and regular dust-on-snow events (e.g., Gleason et al., 2019; Skiles et al., 2015).

565

566 **6. Conclusions**

567 We integrated the widely-used state-of-the-art snow albedo model, the latest version of
568 SNICAR, into the refactored Noah-MP version 5, and evaluated in detail using ground
569 measurements at three Rocky Mountain observation sites. The coupled Noah-MP/SNICAR model
570 physically accounts for the aerosol-snow-radiation interaction, snow grain growth and aging, and
571 effects of snow grain size and shape on snow albedo. The Noah-MP/SNICAR simulation well
572 reproduces the observed broadband, visible, and NIR snow albedo, although it slightly
573 overestimates the visible and broadband snow albedo. The SNICAR scheme significantly
574 improves the temporal variability of snow albedo (particularly in the NIR band) comparing to the
575 semi-physical BATS snow albedo scheme in Noah-MP. The remaining bias in Noah-MP/SNICAR
576 could be attributed to uncertainties in the deposition and evolution of snow impurities and snow
577 aging processes as well as atmospheric forcing and other potential snowpack physics (e.g.,
578 densification), which requires further studies. The individual impacts of snow grain size, non-
579 spherical snow grain shape, and snow impurity on snow albedo and surface radiative forcing have
580 different signs and magnitudes. Overall, the average changes in the broadband snow albedo due to
581 the optimization of fresh snow grain size, the use of non-spherical snow shape, and including LAPs
582 at three stations are 0.018, 0.039, and -0.022. This study substantially enhances the physical
583 representations of snow albedo processes in Noah-MP, which offers a stronger snow albedo
584 modeling capability for future studies considering the wide use of Noah-MP. Future efforts are
585 needed to investigate the climate effects of aerosols in snow via land-atmosphere interaction and
586 snow albedo feedback in fully coupled meteorology-chemistry-snow models.

587

588 **Acknowledgements**

589 The authors thank the reviewers and editor for their helpful comments on improving the paper
590 quality. The authors declare no conflict of interest. T.-S. Lin, C. He, and R. Abolafia-Rosenzweig
591 acknowledge the support of NOAA's Weather Program Office's Subseasonal-to-seasonal (S2S)
592 grant NA22OAR4590503, NOAA's Climate Program Office's Modeling, Analysis, Predictions,
593 and Projections Program (MAPP) grant NA20OAR4310421, and the U.S. Geological Survey
594 (USGS) Water Mission Area's Integrated Water Prediction Program Grant 140G0121F0357. T.-S.
595 Lin would like to acknowledge the high-performance computing support from Cheyenne
596 (doi:10.5065/D6RX99HX) provided by NSF NCAR's Computational and Information Systems
597 Laboratory, sponsored by the National Science Foundation. NSF NCAR is sponsored by the
598 National Science Foundation. Any opinions, findings, conclusions, or recommendations expressed
599 in this publication are those of the authors and do not necessarily reflect the views of the National
600 Science Foundation.

601

Open Research

In situ observed albedo and snow depth from the three study sites are available on https://data.mendeley.com/datasets/5393ck97d9/3 (Abolafia-Rosenzweig et al., 2022b). Simulation data used in this manuscript are available on https://doi.org/10.5281/zenodo.10460675 (Lin et al., 2024). Noah-MP model code updates are publicly available: https://github.com/tslin2/hrldas_snicar.git

References

Abolafia-Rosenzweig, R., He, C., Burns, S. P., & Chen, F. (2021). Implementation and evaluation of a unified turbulence parameterization throughout the canopy and roughness sublayer in Noah-MP Snow Simulations. *Journal of Advances in Modeling Earth Systems, 13*(11). https://doi.org/10.1029/2021ms002665

Abolafia-Rosenzweig, R., He, C., McKenzie Skiles, S., Chen, F., & Gochis, D. (2022a). Evaluation and optimization of snow albedo scheme in Noah-MP Land Surface Model using in situ spectral observations in the Colorado Rockies. *Journal of Advances in Modeling Earth Systems, 14*(10). https://doi.org/10.1029/2022ms003141

Abolafia-Rosenzweig, R., He, C, & Gochis, D. (2022b). "Evaluation and optimization of snow albedo scheme in Noah-MP land surface model using in-situ spectral observations in the Colorado Rockies", Mendeley Data, V3, doi: 10.17632/5393ck97d9.3

Bair, E. H., Rittger, K., Skiles, S. M., & Dozier, J. (2019). An examination of snow albedo estimates from Modis and their impact on snow water equivalent reconstruction. *Water Resources Research, 55*(9), 7826–7842. https://doi.org/10.1029/2019wr024810

Barnett, T. P., Adam, J. C., & Lettenmaier, D. P. (2005). Potential impacts of a warming climate on water availability in snow-dominated regions. Nature, 438(7066), 303–309. https://doi.org/10.1038/nature04141

Brun, E. (1989). Investigation on Wet-Snow metamorphism in respect of Liquid-Water content. *Annals of Glaciology, 13*, 22–26. https://doi.org/10.3189/s0260305500007576

Chen, F., Barlage, M., Tewari, M., Rasmussen, R., Jin, J., Lettenmaier, D., Livneh, B., Lin, C., Miguez-Macho, G., Niu, G., Wen, L., & Yang, Z. (2014). Modeling Seasonal snowpack evolution in the complex terrain and forested Colorado Headwaters Region: A model intercomparison study. *Journal of Geophysical Research: Atmospheres, 119*(24). https://doi.org/10.1002/2014jd022167

Cohen, J., & Rind, D. (1991). The effect of snow cover on the climate. *Journal of Climate, 4*(7), 689–706. https://doi.org/10.1175/1520-0442(1991)004%3C0689:TEOSCO%3E2.0.CO;2

Colbeck, S. C. (1982). An overview of seasonal snow metamorphism. *Reviews of Geophysics, 20*(1), 45–61. https://doi.org/10.1029/rg020i001p00045

Dang, C., Fu, Q., & Warren, S. G. (2016). Effect of snow grain shape on Snow albedo. *Journal of the Atmospheric Sciences, 73*(9), 3573–3583. https://doi.org/10.1175/jas-d-15-0276.1

Dang, C., Zender, C. S., & Flanner, M. G. (2019). Intercomparison and improvement of two-stream shortwave radiative transfer schemes in earth system models for a unified treatment of cryospheric surfaces. *The Cryosphere, 13*(9), 2325–2343. https://doi.org/10.5194/tc-13-2325-2019

Flanner, M. G., Arnheim, J. B., Cook, J. M., Dang, C., He, C., Huang, X., Singh, D., Skiles, S. M., Whicker, C. A., & Zender, C. S. (2021). SNICAR-ADV3: A community tool for modeling spectral snow albedo. *Geoscientific Model Development*, *14*(12), 7673–7704. https://doi.org/10.5194/gmd-14-7673-2021

Flanner, M. G., Shell, K. M., Barlage, M., Perovich, D. K., & Tschudi, M. A. (2011). Radiative forcing and albedo feedback from the Northern Hemisphere cryosphere between 1979 and 2008. *Nature Geoscience*, *4*(3), 151–155. https://doi.org/10.1038/ngeo1062

Flanner, M. G., & Zender, C. S. (2006). Linking snowpack microphysics and albedo evolution. *Journal of Geophysical Research*, *111*(D12). https://doi.org/10.1029/2005jd006834

Flanner, M. G., Zender, C. S., Randerson, J. T., & Rasch, P. J. (2007). Present-day climate forcing and response from black carbon in snow. *Journal of Geophysical Research: Atmospheres*, *112*(D11). https://doi.org/10.1029/2006jd008003

Gleason, K. E., McConnell, J. R., Arienzo, M. M., Chellman, N., & Calvin, W. M. (2019). Four-fold increase in solar forcing on snow in western U.S. burned forests since 1999. *Nature Communications*, *10*(1). https://doi.org/10.1038/s41467-019-09935-y

Hall, A. (2004). The role of surface albedo feedback in climate. *Journal of Climate*, *17*(7), 1550–1568. https://doi.org/10.1175/1520-0442(2004)017<1550:trosaf>2.0.co;2

Hao, D., Bisht, G., Rittger, K., Bair, E., He, C., Huang, H., Dang, C., Stillinger, T., Gu, Y., Wang, H., Qian, Y., & Leung, L. R. (2023). Improving snow albedo modeling in the E3SM Land Model (version 2.0) and assessing its impacts on snow and surface fluxes over the Tibetan Plateau. *Geoscientific Model Development*, *16*(1), 75–94. https://doi.org/10.5194/gmd-16-75-2023

National Weather Service. (2021). Analysis of Record for Calibration: Version 1.1 Sources, Methods, and Verification, https://hydrology.nws.noaa.gov/aorc-historic/Documents/AORC-Version1.1-SourcesMethodsandVerifications.pdf (last access: 17 March 2021).

He, C. (2022). Modelling light-absorbing particle–snow–radiation interactions and impacts on snow albedo: Fundamentals, recent advances and Future Directions. *Environmental Chemistry*, *19*(5), 296–311. https://doi.org/10.1071/en22013

He, C., Chen, F., Abolafia-Rosenzweig, R., Ikeda, K., Liu, C., & Rasmussen, R. (2021). What causes the unobserved early-spring snowpack ablation in convection-permitting WRF modeling over Utah Mountains? *Journal of Geophysical Research: Atmospheres*, *126*(22). https://doi.org/10.1029/2021jd035284

He, C., Chen, F., Barlage, M., Liu, C., Newman, A., Tang, W., Ikeda, K., & Rasmussen, R. (2019a). Can convection-permitting modeling provide decent precipitation for offline high-resolution snowpack simulations over mountains? *Journal of Geophysical Research: Atmospheres*, *124*(23), 12631–12654. https://doi.org/10.1029/2019jd030823

He, C., & Flanner, M. (2020). Snow albedo and radiative transfer: Theory, modeling, and parameterization. *Springer Series in Light Scattering*, 67–133. https://doi.org/10.1007/978-3-030-38696-2_3

He, C., Flanner, M. G., Chen, F., Barlage, M., Liou, K.-N., Kang, S., Ming, J., & Qian, Y. (2018a). Black carbon-induced snow albedo reduction over the Tibetan Plateau: Uncertainties from snow grain shape and aerosol–snow mixing state based on an updated SNICAR model. *Atmospheric Chemistry and Physics*, *18*(15), 11507–11527. https://doi.org/10.5194/acp-18-11507-2018

He, C., Flanner, M., Lawrence, D. M., & Gu, Y. (2023a). New features and enhancements in Community Land Model (CLM5) snow albedo modeling: Description, sensitivity, and evaluation. *ESSOAR*. https://doi.org/10.22541/essoar.168626390.01530324/v1

He, C., Li, Q., Liou, K., Takano, Y., Gu, Y., Qi, L., Mao, Y., & Leung, L. R. (2014). Black carbon radiative forcing over the Tibetan Plateau. *Geophysical Research Letters*, *41*(22), 7806–7813. https://doi.org/10.1002/2014gl062191

He, C., Liou, K., Takano, Y., Chen, F., & Barlage, M. (2019b). Enhanced snow absorption and albedo reduction by dust-snow internal mixing: Modeling and parameterization. *Journal of Advances in Modeling Earth Systems*, *11*(11), 3755–3776. https://doi.org/10.1029/2019ms001737

He, C., Liou, K., Takano, Y., Yang, P., Qi, L., & Chen, F. (2018b). Impact of grain shape and multiple black carbon internal mixing on snow albedo: Parameterization and radiative effect analysis. *Journal of Geophysical Research: Atmospheres*, *123*(2), 1253–1268. https://doi.org/10.1002/2017jd027752

He, C., Takano, Y., Liou, K.-N., Yang, P., Li, Q., & Chen, F. (2017). Impact of snow grain shape and black carbon–snow internal mixing on snow optical properties: Parameterizations for climate models. *Journal of Climate*, *30*(24), 10019–10036. https://doi.org/10.1175/jcli-d-17-0300.1

He, C., Valayamkunnath, P., Barlage, M., Chen, F., Gochis, D., Cabell, R., Schneider, T., Rasmussen, R., Niu, G.-Y., Yang, Z.-L., Niyogi, D., & Ek, M. (2023b). Modernizing the open-source community Noah with multi-parameterization options (Noah-MP) land surface model (version 5.0) with enhanced modularity, interoperability, and applicability. *Geoscientific Model Development*, *16*(17), 5131–5151. https://doi.org/10.5194/gmd-16-5131-2023

He, C., Valayamkunnath, P., Barlage, M., Chen, F., Gochis, D., Cabell, R., Schneider, T., Rasmussen, R., Niu, G. Y., Yang, Z. L., Niyogi, D., & Ek, M. (2023c). The Community Noah-MP Land Surface Modeling System Technical Description Version 5.0, NCAR Tech. Note, No. NCAR/TN-575+STR, https://doi.org/10.5065/ew8g-yr95

Ikeda, K., Rasmussen, R., Liu, C., Newman, A., Chen, F., Barlage, M., Gutmann, E., Dudhia, J., Dai, A., Luce, C., & Musselman, K. (2021). Snowfall and snowpack in the western U.S. as captured by convection permitting climate simulations: Current climate and pseudo global warming future climate. *Climate Dynamics*, *57*(7–8), 2191–2215. https://doi.org/10.1007/s00382-021-05805-w

Lawrence, D. M., Fisher, R. A., Koven, C. D., Oleson, K. W., Swenson, S., Bonan, G. B., Collier, N., Ghimire, B., Van Kampenhout, L., Kennedy, D., Kluzek, E., Li, F., Li, H., Lombardozzi, D., Riley, W. J., Sacks, W. J., Shi, M., Vertenstein, M., Wieder, W. R., . . . Zeng, X. (2019). The Community Land Model Version 5: Description of new features, benchmarking, and impact of forcing uncertainty. *Journal of Advances in Modeling Earth Systems*, *11*(12), 4245–4287. https://doi.org/10.1029/2018ms001583

Lin, T.-S., He, C., Abolafia-Rosenzweig, R., Chen, F., Wang, W., Barlage, M., & Gochis, D. (2024). Model dataset for the journal publication titled "Implementation and evaluation of SNICAR snow albedo scheme in Noah-MP (version 5.0) land surface model" [Data set]. Zenodo. https://doi.org/10.5281/zenodo.10460675

Liou, K. N., Takano, Y., He, C., Yang, P., Leung, L. R., Gu, Y., & Lee, W. L. (2014). Stochastic parameterization for light absorption by internally mixed BC/dust in snow grains for

application to climate models. *Journal of Geophysical Research: Atmospheres*, *119*(12), 7616–7632. https://doi.org/10.1002/2014jd021665

Liu, C., Ikeda, K., Rasmussen, R., Barlage, M., Newman, A. J., Prein, A. F., Chen, F., Chen, L., Clark, M., Dai, A., Dudhia, J., Eidhammer, T., Gochis, D., Gutmann, E., Kurkute, S., Li, Y., Thompson, G., & Yates, D. (2016). Continental-scale convection-permitting modeling of the current and future climate of North America. *Climate Dynamics*, *49*(1–2), 71–95. https://doi.org/10.1007/s00382-016-3327-9

Liu, L., Ma, Y., Menenti, M., Su, R., Yao, N., & Ma, W. (2021). Improved parameterization of snow albedo in Noah coupled with weather research and forecasting: Applicability to snow estimates for the Tibetan Plateau. *Hydrology and Earth System Sciences*, *25*(9), 4967–4981. https://doi.org/10.5194/hess-25-4967-2021

Liu, L., Menenti, M., & Ma, Y. (2022). Evaluation of albedo schemes in WRF coupled with Noah-MP on the Parlung No. 4 glacier. *Remote Sensing*, *14*(16), 3934. https://doi.org/10.3390/rs14163934

Manninen, T., Anttila, K., Jääskeläinen, E., Riihelä, A., Peltoniemi, J., Räisänen, P., Lahtinen, P., Siljamo, N., Thölix, L., Meinander, O., Kontu, A., Suokanerva, H., Pirazzini, R., Suomalainen, J., Hakala, T., Kaasalainen, S., Kaartinen, H., Kukko, A., Hautecoeur, O., & Roujean, J.-L. (2021). Effect of small-scale snow surface roughness on snow albedo and reflectance. *The Cryosphere*, *15*(2), 793–820. https://doi.org/10.5194/tc-15-793-2021

Nash, J. E., & Sutcliffe, J. V. (1970). River flow forecasting through conceptual models part I — a discussion of Principles. *Journal of Hydrology*, *10*(3), 282–290. https://doi.org/10.1016/0022-1694(70)90255-6

Niu, G.-Y., Yang, Z.-L., Mitchell, K. E., Chen, F., Ek, M. B., Barlage, M., Kumar, A., Manning, K., Niyogi, D., Rosero, E., Tewari, M., & Xia, Y. (2011). The community Noah Land Surface Model with multiparameterization options (Noah-MP): 1. model description and evaluation with local-scale measurements. *Journal of Geophysical Research*, *116*(D12). https://doi.org/10.1029/2010jd015139

Niu, H., Kang, S., Zhang, Y., Shi, X., Shi, X., Wang, S., Li, G., Yan, X., Pu, T., & He, Y. (2017). Distribution of light-absorbing impurities in snow of glacier on Mt. Yulong, southeastern Tibetan Plateau. *Atmospheric Research*, *197*, 474–484. https://doi.org/10.1016/j.atmosres.2017.07.004

Oleson, K., Lawrence, D. M., Bonan, G. B., Drewniak, B., Huang, M., Koven, C. D., … Yang, Z. -L. (2013). *Technical description of version 4.5 of the Community Land Model (CLM)* (No. NCAR/TN-503+STR). doi:10.5065/D6RR1W7M

Painter, T. H., Rittger, K., McKenzie, C., Slaughter, P., Davis, R. E., & Dozier, J. (2009). Retrieval of subpixel snow covered area, grain size, and albedo from Modis. *Remote Sensing of Environment*, *113*(4), 868–879. https://doi.org/10.1016/j.rse.2009.01.001

Picard, G., Libois, Q., & Arnaud, L. (2016). Refinement of the ice absorption spectrum in the visible using radiance profile measurements in Antarctic Snow. *The Cryosphere*, *10*(6), 2655–2672. https://doi.org/10.5194/tc-10-2655-2016

Qian, Y., Wang, H., Zhang, R., Flanner, M. G., & Rasch, P. J. (2014). A sensitivity study on modeling black carbon in snow and its radiative forcing over the Arctic and northern China. *Environmental Research Letters*, *9*(6), 064001. https://doi.org/10.1088/1748-9326/9/6/064001

779 Qian, Y., Yasunari, T. J., Doherty, S. J., Flanner, M. G., Lau, W. K., Ming, J., Wang, H., Wang,
780 M., Warren, S. G., & Zhang, R. (2015). Light-absorbing particles in snow and ice:
781 Measurement and modeling of climatic and hydrological impact. *Advances in Atmospheric*
782 *Sciences*, *32*(1), 64–91. https://doi.org/10.1007/s00376-014-0010-0
783 Randles, C. A., da Silva, A. M., Buchard, V., Colarco, P. R., Darmenov, A., Govindaraju, R.,
784 Smirnov, A., Holben, B., Ferrare, R., Hair, J., Shinozuka, Y., & Flynn, C. J. (2017). The
785 merra-2 aerosol reanalysis, 1980 onward. part I: System description and data assimilation
786 evaluation. *Journal of Climate*, *30*(17), 6823–6850. https://doi.org/10.1175/jcli-d-16-
787 0609.1
788 Rasmussen, R. M., Chen, F., Liu, C. H., Ikeda, K., Prein, A., Kim, J., Schneider, T., Dai, A.,
789 Gochis, D., Dugger, A., Zhang, Y., Jaye, A., Dudhia, J., He, C., Harrold, M., Xue, L.,
790 Chen, S., Newman, A., Dougherty, E., … Miguez-Macho, G. (2023). CONUS404: The
791 ncar–USGS 4-km long-term regional hydroclimate reanalysis over the CONUS. *Bulletin of*
792 *the American Meteorological Society*, *104*(8). https://doi.org/10.1175/bams-d-21-0326.1
793 Robledano, A., Picard, G., Dumont, M., Flin, F., Arnaud, L., & Libois, Q. (2023). Unraveling the
794 optical shape of snow. *Nature Communications*, *14*(1). https://doi.org/10.1038/s41467-
795 023-39671-3
796 Skiles, S. M., Flanner, M., Cook, J. M., Dumont, M., & Painter, T. H. (2018). Radiative forcing
797 by light-absorbing particles in snow. *Nature Climate Change*, *8*(11), 964–971.
798 https://doi.org/10.1038/s41558-018-0296-5
799 Skiles, S. M., & Painter, T. H. (2019). Toward understanding direct absorption and grain size
800 feedbacks by dust radiative forcing in snow with coupled snow physical and radiative
801 transfer modeling. *Water Resources Research*, *55*(8), 7362–7378.
802 https://doi.org/10.1029/2018wr024573
803 Skiles, S. M., Painter, T. H., Belnap, J., Holland, L., Reynolds, R. L., Goldstein, H. L., & Lin, J.
804 (2015). Regional variability in dust-on-snow processes and impacts in the upper Colorado
805 River Basin. *Hydrological Processes*, *29*(26), 5397–5413.
806 https://doi.org/10.1002/hyp.10569
807 Thackeray, C. W., & Fletcher, C. G. (2016). Snow albedo feedback. *Progress in Physical*
808 *Geography: Earth and Environment*, *40*(3), 392–408.
809 https://doi.org/10.1177/0309133315620999
810 Toon, O. B., McKay, C. P., Ackerman, T. P., & Santhanam, K. (1989). Rapid calculation of
811 radiative heating rates and photodissociation rates in inhomogeneous multiple scattering
812 atmospheres. *Journal of Geophysical Research: Atmospheres*, *94*(D13), 16287–16301.
813 https://doi.org/10.1029/jd094id13p16287
814 Verseghy, D. L. (2007). Class-A Canadian land surface scheme for GCMS. I. Soil Model.
815 *International Journal of Climatology*, *11*(2), 111–133.
816 https://doi.org/10.1002/joc.3370110202
817 Wang, W., He, C., Moore, J., Wang, G., & Niu, G. (2022). Physics-based narrowband optical
818 parameters for snow albedo simulation in climate models. *Journal of Advances in*
819 *Modeling Earth Systems*, *14*(1). https://doi.org/10.1029/2020ms002431
820 Wang, W., Yang, K., Zhao, L., Zheng, Z., Lu, H., Mamtimin, A., Ding, B., Li, X., Zhao, L., Li,
821 H., Che, T., & Moore, J. C. (2020). Characterizing surface albedo of shallow fresh snow
822 and its importance for snow ablation on the interior of the Tibetan Plateau. *Journal of*
823 *Hydrometeorology*, *21*(4), 815–827. https://doi.org/10.1175/jhm-d-19-0193.1

824 Warren, S. G. (1982). Optical properties of snow. *Reviews of Geophysics*, *20*(1), 67–89.
825 https://doi.org/10.1029/rg020i001p00067
826 Warren, S. G. (1984). Optical constants of ice from the ultraviolet to the microwave. Applied
827 Optics, 23(8), 1206. https://doi.org/10.1364/ao.23.001206
828 Warren, S. G., & Brandt, R. E. (2008). Optical constants of ice from the ultraviolet to the
829 microwave: A revised compilation. *Journal of Geophysical Research: Atmospheres*,
830 *113*(D14). https://doi.org/10.1029/2007jd009744
831 Warren, S. G., & Wiscombe, W. J. (1980). A model for the spectral albedo of snow. II: Snow
832 containing atmospheric aerosols. *Journal of the Atmospheric Sciences*, *37*(12), 2734–2745.
833 https://doi.org/10.1175/1520-0469(1980)037<2734:amftsa>2.0.co;2
834 Wiscombe, W. J., & Warren, S. G. (1980). A model for the spectral albedo of snow. I: Pure
835 snow. *Journal of the Atmospheric Sciences*, *37*(12), 2712–2733.
836 https://doi.org/10.1175/1520-0469(1980)037<2712:amftsa>2.0.co;2
837 Yang, Z.-L., Dickinson, R. E., Robock, A., & Vinnikov, K. Y. (1997). Validation of the snow
838 submodel of the biosphere–atmosphere transfer scheme with Russian snow cover and
839 meteorological observational data. *Journal of Climate*, *10*(2), 353–373.
840 https://doi.org/10.1175/1520-0442(1997)010<0353:votsso>2.0.co;2
841 Yang, Z.-L., Niu, G.-Y., Mitchell, K. E., Chen, F., Ek, M. B., Barlage, M., Longuevergne, L.,
842 Manning, K., Niyogi, D., Tewari, M., & Xia, Y. (2011). The community Noah Land
843 Surface Model with multiparameterization options (Noah-MP): 2. evaluation over Global
844 River basins. *Journal of Geophysical Research*, *116*(D12).
845 https://doi.org/10.1029/2010jd015140
846 Xiao, M., Mahanama, S. P., Xue, Y., Chen, F., & Lettenmaier, D. P. (2021). Modeling snow
847 ablation over the mountains of the Western United States: Patterns and controlling factors.
848 *Journal of Hydrometeorology*, *22*(2), 297–311. https://doi.org/10.1175/jhm-d-19-0198.1
849 Zhang, R., Wang, H., Fu, Q., Rasch, P. J., & Wang, X. (2019). Unraveling driving forces
850 explaining significant reduction in satellite-inferred Arctic surface albedo since the 1980s.
851 *Proceedings of the National Academy of Sciences*, *116*(48), 23947–23953.
852 https://doi.org/10.1073/pnas.1915258116
853